Nonreciprocal and dispersive solutions of a magnetoelectroelastic slab waveguide

Zhengliu Zhou[1,*] and Scott Keller[2]

[1] *Skyworks Solutions Inc., Irvine, California 92617, USA*

[2] *Department of Mechanical Engineering, University of California, Riverside, Riverside, California 92521, USA*

(Received 29 June 2022; revised 8 November 2023; accepted 22 December 2023; published 9 January 2024)

We apply the transfer-matrix method to the equations of wave motion in a magnetoelectroelastic (MEE) solid and compute the dispersion of an MEE slab waveguide. The dispersion curves exhibit periodic regions of resonance, where the group velocity approaches zero and the mechanical coupling is reinforced. Inside these regions, the group velocity of higher-order modes can slow to $10^3 - 10^4$ m/s. Substantial nonreciprocity, e.g., a 14.2% difference in phase velocity between forward and backward waves, can be realized within an MEE waveguide at select directions and frequencies. This suggests MEE waveguides as a potential alternative for magnet-free nonreciprocal devices.

DOI: 10.1103/PhysRevApplied.21.014013

I. INTRODUCTION

Magnetoelectroelastic (MEE) material typically consists of a piezoelectric phase and a piezomagnetic phase [1] that are connected in a way such that the mechanical strain is coupled between each other. It has received considerable attention because of its magnetoelectric (ME) coupling that are of great potential in a wide range of engineering applications, such as energy-efficient memory devices [2], magnetic sensors with extremely low equivalent magnetic noise [3] and acoustically driven antenna whose size is minute compared to the electromagnetic (EM) wavelength in free space [4]. Additionally, in condensed-matter physics, a noteworthy example making use of MEE material is the so-called photonic topological insulator, which has bosonic broken time-reversal symmetry due to the Tellegen ME coupling [5].

To maximize ME coupling, research has shown that the laminate MEE composite made by stacking up piezoelectric and piezomagnetic layers provides a viable means due to the relatively large interface area and effective strain transfer enabled therein [6]. Like other types of stratified composite materials, the MEE composite has been extensively studied in terms of their guided wave-propagation properties [7], but mostly the focus is on the elastic wave and the quasistatic approximation is assumed [8]. In this case, the electric field (E field) and the magnetic field (H field) are decoupled, each represented by the gradient of a scalar potential, i.e., $\underline{E} = -\nabla\phi_e$, $\underline{H} = -\nabla\phi_m$ and thus the propagating EM waves cannot be described. To understand the EM wave propagation in MEE composites whose dimensions are comparable to EM wavelength, we must solve the equation of mechanical motion and Maxwell's equations simultaneously, which is very challenging in general. For infinitely extended layered media, however, the two sets of partial differential equations (PDEs) can be simplified as ordinary differential equations (ODE) that become solvable with the help of the transfer-matrix method (TMM).

In light of the field continuity at the interface between adjacent layers, TMM relates by multiplication of the transfer matrices the fields on the outermost boundaries where boundary conditions are prescribed. It has been widely used for studying both elastic waves and EM waves, such as Lamb wave in fiber-reinforced polymers [9] and the light traveling in dielectric slab waveguide [10]. Nonetheless, so far TMM has not been used for MEE laminate composites, in which elastic wave and EM wave are intrinsically coupled. In this report, we first derive the general formulation of TMM incorporating MEE constitutive relations, and then obtain the dispersion relations. We find that in the dispersion curves, there exist periodic resonances, which strengthen piezoelectric and piezomagnetic response, hence enhancing ME coupling effects. In these resonance regions, the wave number of propagation increases rapidly and thus the group velocity tends to zero. Further looking into a typical resonance region reveals that modes of various orders are present. Lower-order modes ($n = 0, 1$) are highly dispersive, whereas high-order modes ($n \geq 2$) are dispersionless. Of note, we show that by optimizing the constituent layers' local material coordinates, considerable nonreciprocity can be achieved in the MEE waveguide around the resonance regions, as demonstrated by 14.2% difference in phase velocity between waves traveling along opposite directions.

*zhouzl07@gmail.com

II. THEORY

To begin with, the elastodynamic equation of motion can be written as

$$\nabla \cdot \underline{\underline{T}} = \rho \frac{\partial^2 \underline{u}}{\partial t^2} \rightarrow \nabla \cdot \underline{\underline{T}} = \rho \frac{\partial \underline{v}}{\partial t}, \tag{1}$$

where $\underline{\underline{T}}$ is the stress tensor, ρ is the density, $\underline{u}$ is the displacement, and $\underline{v} = \partial \underline{u}/\partial t$ is the velocity. For small deformation, the strain-displacement relation is

$$\underline{\underline{S}} = \frac{1}{2}((\nabla \underline{u}) + (\nabla \underline{u})^T) \quad \rightarrow \quad \frac{\partial \underline{\underline{S}}}{\partial t} = \frac{1}{2}((\nabla \underline{v}) + (\nabla \underline{v})^T), \tag{2}$$

where $\underline{\underline{S}}$ is the strain tensor.

On the other hand, the EM fields are characterized by the two curl equations of Maxwell's equations:

$$\nabla \times \underline{E} = -\frac{\partial \underline{B}}{\partial t}, \tag{3}$$

$$\nabla \times \underline{H} = \frac{\partial \underline{D}}{\partial t}, \tag{4}$$

where $\underline{E}$ and $\underline{H}$ are E field and H field, respectively; $\underline{B}$ and $\underline{D}$ are the magnetic flux density and electric flux density, respectively.

We have made the following assumptions in the equations presented: in Eq. (1), there is no body force; in Eq. (4), there is no impressed current source. Further, we assume the motion is time harmonic and the convention of $\exp(j\omega t)$ is taken. Consequently, Eqs. (1)–(4) can be rewritten as

$$\begin{aligned} \nabla \cdot \underline{\underline{T}} - j\omega\rho\underline{v} &= 0, \\ j\omega\underline{\underline{S}} - \frac{1}{2}\left((\nabla\underline{v}) + (\nabla\underline{v})^T\right) &= 0, \\ \nabla \times \underline{E} + j\omega\underline{B} &= 0, \\ \nabla \times \underline{H} - j\omega\underline{D} &= 0. \end{aligned} \tag{5}$$

For plane waves, the gradient operator can be replaced with $-j\,\underline{k}$ where $\underline{k}$ is the wavevector and its magnitude is $k \in \mathbb{C}$. Thus, Eq. (5) can be further simplified as

$$\begin{cases} -j\,\underline{k} \cdot \underline{\underline{T}} - j\omega\rho\underline{v} = 0 \\ j\omega\underline{\underline{S}} + \frac{j}{2}\left((\underline{kv}) + (\underline{kv})^T\right) = 0 \\ -j\,\underline{k} \times \underline{E} + j\omega\underline{B} = 0 \\ -j\,\underline{k} \times \underline{H} - j\omega\underline{D} = 0 \end{cases} \rightarrow \begin{cases} \frac{1}{\omega}\mathbf{N}\underline{\underline{T}} + \rho\underline{v} = 0 \\ \underline{\underline{S}} + \frac{1}{\omega}\mathbf{N}^T\underline{v} = 0 \\ \frac{1}{\omega}\mathbf{K}\underline{E} - \underline{B} = 0 \\ \frac{1}{\omega}\mathbf{K}\underline{H} + \underline{D} = 0 \end{cases} \tag{6}$$

where we have used the Voigt notation for both stress and strain, i.e., $\underline{\underline{T}} = \begin{bmatrix} T_1 & T_2 & T_3 & T_4 & T_5 & T_6 \end{bmatrix}^T$ and $\underline{\underline{S}} = \begin{bmatrix} S_1 & S_2 & S_3 & S_4 & S_5 & S_6 \end{bmatrix}^T$, and $\mathbf{N}$, $\mathbf{K}$ are defined by the following:

$$\mathbf{N} = \begin{bmatrix} k_x & \cdot & \cdot & \cdot & k_z & k_y \\ \cdot & k_y & \cdot & k_z & \cdot & k_x \\ \cdot & \cdot & k_z & k_y & k_x & \cdot \end{bmatrix},$$

$$\mathbf{K} = \begin{bmatrix} \cdot & -k_z & k_y \\ k_z & \cdot & -k_x \\ -k_y & k_x & \cdot \end{bmatrix}$$

in which k_x, k_y, k_z are the components of k along x, y, and z axis, respectively.

At this point, we substitute into Eq. (6) the constitutive relations of the MEE materials:

$$\begin{cases} \underline{\underline{S}} = \mathbf{s}\underline{\underline{T}} + \mathbf{d}^T\underline{E} + \mathbf{q}^T\underline{H} \\ \underline{D} = \mathbf{d}\underline{\underline{T}} + \boldsymbol{\varepsilon}\underline{E} + \boldsymbol{\xi}\underline{H} \\ \underline{B} = \mathbf{q}\underline{\underline{T}} + \boldsymbol{\zeta}\underline{E} + \boldsymbol{\mu}\underline{H} \end{cases} \tag{7}$$

where $\mathbf{s}$ is the 6×6 compliance matrix (inverse of the stiffness matrix), and the 3×6 matrix $\mathbf{d}$ and $\mathbf{q}$ describe the piezoelectric and piezomagnetic coupling, respectively; $\boldsymbol{\varepsilon}$ and $\boldsymbol{\mu}$ are the permittivity and permeability matrices; both $\boldsymbol{\xi}$ and $\boldsymbol{\zeta}$ are termed magnetoelectric coupling matrices with $\boldsymbol{\xi}^* = \boldsymbol{\zeta}^T$ for lossless materials [11], i.e., one is the Hermitian transpose of the other. Here we focus on cases where the entries of $\boldsymbol{\xi}$ are real valued. The governing equations are therefore of the following form ($\mathbf{I}$ is the identity matrix of size indicated by the subscript):

$$\underbrace{\begin{bmatrix} \mathbf{s} & \frac{1}{\omega}\mathbf{N}^T & \mathbf{d}^T & \mathbf{q}^T \\ \frac{1}{\omega}\mathbf{N} & \rho\mathbf{I}_{3\times3} & \mathbf{0}_{3\times3} & \mathbf{0}_{3\times3} \\ \mathbf{d} & \mathbf{0}_{3\times3} & \boldsymbol{\varepsilon} & \frac{1}{\omega}\mathbf{K} + \boldsymbol{\xi} \\ \mathbf{q} & \mathbf{0}_{3\times3} & -\frac{1}{\omega}\mathbf{K} + \boldsymbol{\zeta} & \boldsymbol{\mu} \end{bmatrix}}_{\mathbf{A}} \underbrace{\begin{bmatrix} \underline{\underline{T}} \\ \underline{v} \\ \underline{E} \\ \underline{H} \end{bmatrix}}_{\underline{x}} = \underline{0}. \tag{8}$$

Since $\mathbf{K}^T = -\mathbf{K}$, we note that $((1/\omega)\mathbf{K} + \boldsymbol{\xi})^T = -(1/\omega)\mathbf{K} + \boldsymbol{\zeta}$. As a result, $\mathbf{A}$ is indeed symmetric.

The formulation of TMM requires converting Eq. (8) into equations of variables that are continuous at the interfaces between layers. Let us assume these interfaces are perpendicular to the z axis and split the variables in $\underline{x}$ into two groups: $\underline{x}_a = \begin{bmatrix} T_1 & T_2 & T_6 & E_z & H_z \end{bmatrix}^T$ and $\underline{x}_b = \begin{bmatrix} T_3 & E_x & T_4 & E_y & T_5 & v_x & v_z & H_y & v_y & H_x \end{bmatrix}^T$, so that

$\underline{x}_b$ is continuous across the interface while $\underline{x}_a$ is not necessarily so. Equation (8) can then be rearranged as

$$\underbrace{\begin{bmatrix}\mathbf{Q}_{11} & \mathbf{Q}_{12}\\ \mathbf{Q}_{12}^T & \mathbf{Q}_{22}\end{bmatrix}}_{\mathbf{Q}}\begin{bmatrix}\underline{x}_a\\ \underline{x}_b\end{bmatrix} = \underline{0} \rightarrow \begin{matrix}\mathbf{Q}_{11}\underline{x}_a + \mathbf{Q}_{12}\underline{x}_b = \underline{0}\\ \mathbf{Q}_{12}^T\underline{x}_a + \mathbf{Q}_{22}\underline{x}_b = \underline{0}\end{matrix}, \tag{9}$$

where $\mathbf{Q}_{11}$, $\mathbf{Q}_{12}(k_x, k_y, \omega)$, and $\mathbf{Q}_{22}(k_x, k_y, k_z, \omega)$ have size 5×5, 5×10 and 10×10, respectively. The expression of $\mathbf{Q}$ can be found in the Appendix.

Assuming $\mathbf{Q}_{11}$ is invertible,[12] we can eliminate $\underline{x}_a$ by substituting $\underline{x}_a = -\mathbf{Q}_{11}^{-1}\mathbf{Q}_{12}\underline{x}_b$ into the second equation in Eq. (9):

$$(-\mathbf{Q}_{12}^T\mathbf{Q}_{11}^{-1}\mathbf{Q}_{12} + \mathbf{Q}_{22})\underline{x}_b = \underline{0}. \tag{10}$$

Moreover, if we write $\mathbf{Q}_{22}$ as a sum of two matrices: $\mathbf{Q}_{22}(k_x, k_y, k_z, \omega) = \mathbf{Q}_{22}^z(k_z, \omega) + \mathbf{Q}_{22}^c(k_x, k_y, \omega)$, in which $\mathbf{Q}_{22}^z$ is a function of ω and k_z, whereas $\mathbf{Q}_{22}^c$ involves ω, k_x, k_y, then Eq. (10) can be written as the following:

$$\mathbf{Q}_{22}^z(k_z, \omega)\underline{x}_b = (\mathbf{Q}_{12}^T(k_x, k_y, \omega)\mathbf{Q}_{11}^{-1}\mathbf{Q}_{12}(k_x, k_y, \omega) - \mathbf{Q}_{22}^c(k_x, k_y, \omega))\underline{x}_b. \tag{11}$$

Selecting $\mathbf{Q}_{22}^z$ as indicated in the Appendix, it is possible to multiply by a permutation matrix $\mathbf{P}$ on both sides such that $\mathbf{P}Q_{22}^z = -j\,k_z\mathbf{I}$. Then we have

$$\begin{aligned}\mathbf{P}Q_{22}^z\underline{x}_b &= \underbrace{\mathbf{P}(\mathbf{Q}_{12}^T\mathbf{Q}_{11}^{-1}\mathbf{Q}_{12} - \mathbf{Q}_{22}^c)}_{\mathbf{M}(k_x,k_y,\omega)}\underline{x}_b\\ \Rightarrow -j\,k_z\mathbf{I}\underline{x}_b &= \mathbf{M}(k_x, k_y, \omega)\underline{x}_b\end{aligned} \tag{12}$$

where $\mathbf{I}$ is the identity matrix, $\mathbf{M}$ is the transfer matrix of size 10×10. For simplicity, we assume the solution is constant in the y direction and thus $\partial/\partial y = 0$. With the ansatz that for a plane wave, we would have $\underline{x}_b = \underline{\hat{x}}_b(z)\exp(-j\,k_x x)$, Eq. (12) can be further reduced to the following:

$$\frac{d}{dz}\underline{\hat{x}}_b(z) = \mathbf{M}(k_x, k_y, \omega)\underline{\hat{x}}_b(z). \tag{13}$$

Given that $\mathbf{M}$ is symmetric, the ten eigenvalues, i.e., wave numbers, can be grouped into five pairs, corresponding to the five eigenmodes that can exist in MEE materials, among which are three quasiacoustic modes and two quasi-EM modes [13]. Accordingly, the ten eigenvectors specify the eigenmodes' field profile, which are thus independent. This indicates $\mathbf{M}$ is diagonalizable and can be written as $\mathbf{M} = \mathbf{U}\Lambda\mathbf{U}^{-1}$, where $\mathbf{\Lambda} = \mathrm{diag}\begin{bmatrix}\lambda_1 & \lambda_2 & \ldots & \lambda_{10}\end{bmatrix}$ with λ_i, $i = 1, 2, \ldots, 10$ being the eigenvalues of $\mathbf{M}$, and the columns of $\mathbf{U}$ are eigenvectors.

And we find from the theory of ordinary differential equation the solution to Eq. (13) is

$$\underline{\hat{x}}_b(z) = \exp(\mathbf{M}(z - z_0))\underline{\hat{x}}_b(z_0), \tag{14}$$

where $\exp(\mathbf{M}z)$ can be decomposed into the following form:

$$\exp(\mathbf{M}z) = \mathbf{U}\exp(\mathbf{\Lambda}z)\mathbf{U}^{-1}. \tag{15}$$

III. ANALYSIS

The multilayered waveguide, an MEE composite structure, is shown in Fig. 1, where the piezoelectric and the piezomagnetic phases of equal thickness, $t = 2.5\ \mu$m, are stacked alternately. The total thickness of the MEE composite is 0.5 mm. The solid is sandwiched by two layers of a fictitious material with permittivity and permeability ε_0

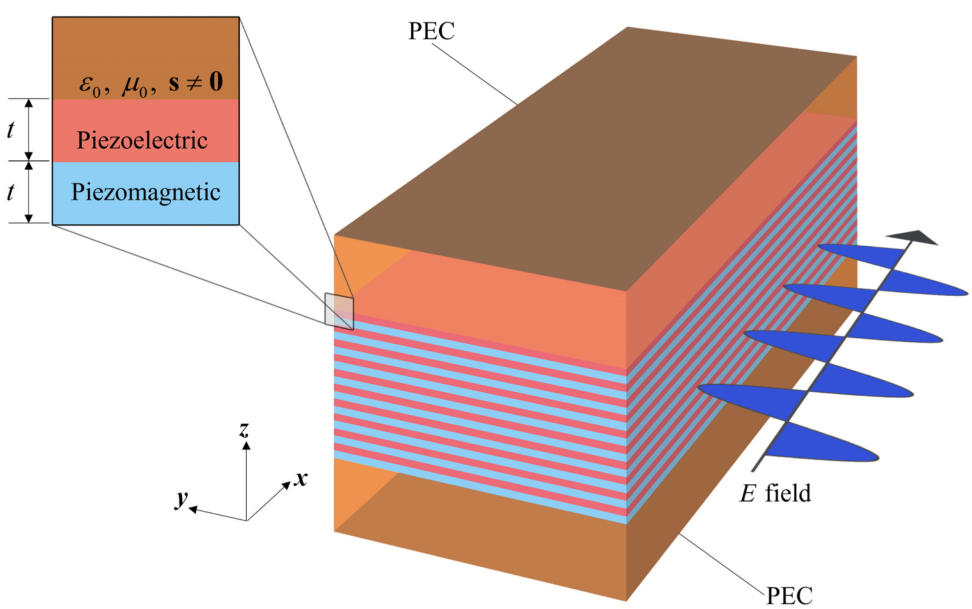

FIG. 1. Schematic of the magnetoelectroelastic waveguide composed of alternating piezoelectric and piezomagnetic layers. PEC stands for Perfect Electric Conductor whose electric conductivity is infinitely large. For the current study, both the piezoelectric and piezomagnetic layers are of equal thickness, i.e., 2.5 and 1.25 um, respectively, in the two cases studied here. The total thickness of this slab waveguide is 0.5 mm.

and μ_0, respectively. The fictitious sandwich layers have a nonsingular stiffness matrix; however, the magnitude of each entry in the stiffness matrix is minuscule (10 orders of magnitude smaller) compared to that of the piezoelectric and piezomagnetic stiffnesses. For this structure, due to interfacial continuity, the field at the bottom surface $z = z_1$ can be associated with that at the top surface $z = z_n$ by applying Eq. (14) to each layer of the entire stack:

$$\hat{\underline{x}}_b(z_n) = \underbrace{\exp(\mathbf{M}_n(z_n - z_{n-1}))\exp(\mathbf{M}_{n-1}(z_{n-1} - z_{n-2}))\cdots\exp(\mathbf{M}_2(z_2 - z_1))}_{\mathbf{T}(k_x,\omega)}\hat{\underline{x}}_b(z_1). \tag{16}$$

If we are mainly concerned about the so-called confined modes, where the EM fields outside of the waveguide (i.e., in the fictitious material) are evanescent along the z axis, we can define the top and bottom as perfect electric conductors (PEC), where tangential E fields and normal H fields vanish. This makes sense given the sharp contrast of the EM properties between the fictitious material and the piezoelectric and piezomagnetic materials. For well posedness, we are also required to define mechanical boundary conditions. To this end, traction-free surfaces can be imposed on each boundary. Hence, with the boundary conditions: $T_3 = T_4 = T_5 = 0,\ E_x = E_y = 0$ at $z = z_n$ and $z = z_1$, (16) is written explicitly as below:

$$\left.\begin{bmatrix} 0 \\ 0 \\ 0 \\ 0 \\ 0 \\ v_x \\ v_z \\ H_y \\ v_y \\ H_x \end{bmatrix}\right|_{z=z_n} = \begin{bmatrix} \mathbf{T}_{11} & \mathbf{T}_{12} \\ \mathbf{T}_{21} & \mathbf{T}_{22} \end{bmatrix} \left.\begin{bmatrix} 0 \\ 0 \\ 0 \\ 0 \\ 0 \\ v_x \\ v_z \\ H_y \\ v_y \\ H_x \end{bmatrix}\right|_{z=z_1}$$

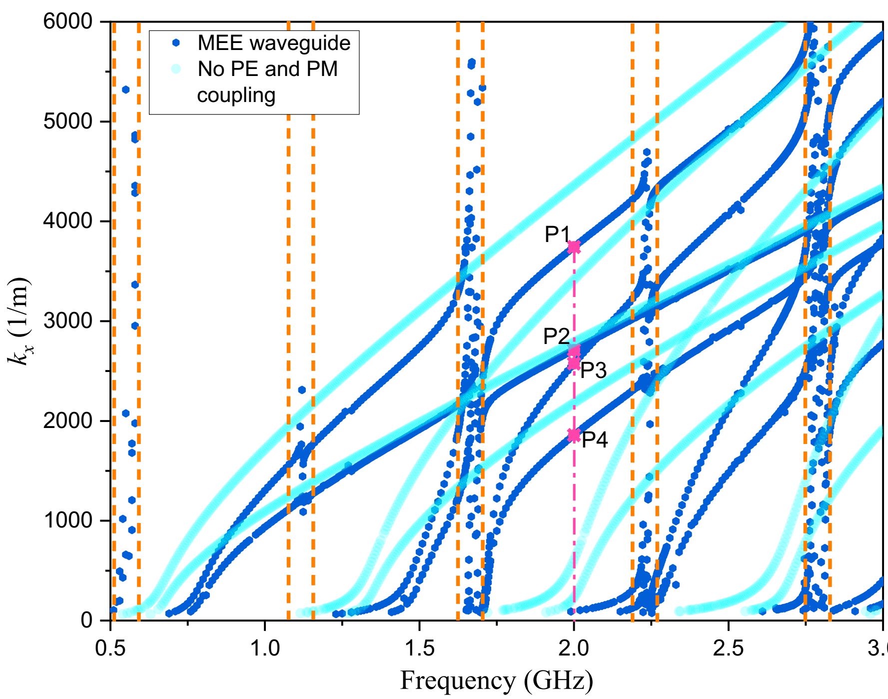

FIG. 2. The dispersion curves of the confined modes in the MEE waveguide (dark blue), in reference to the case with no piezoelectric and piezomagnetic coupling (cyan); the mode profile of the four points P1 ($k_x = 3743.4\ \mathrm{m}^{-1}$), P2 ($k_x = 2713.2\ \mathrm{m}^{-1}$), P3 ($k_x = 2575.6\ \mathrm{m}^{-1}$), P4 ($k_x = 1858.7\ \mathrm{m}^{-1}$) at 2 GHz are plotted in Fig. 3. The regions enclosed by orange dashed lines highlight the k_x values that change rapidly due to the resonance condition governed by Eq. (18).

where **T** is represented by four block submatrices of 5×5. For the solution to be nontrivial, i.e., v_x, v_z, H_y, v_y, H_x not all equal to zero, we must have

$$\det(\mathbf{T}_{12}) \equiv f(k_x, \omega) = 0 \tag{17}$$

satisfied for all k_x of the guided modes at an arbitrarily given frequency.

In our study, $BaTiO_3$ and $CoFe_2O_4$ are used for the piezoelectric layers and piezomagnetic layers, respectively, with properties taken from Ref. [14]. Both are poled along the z axis and isotropic across the x-y plane. The dispersion curve is then numerically computed and plotted in Fig. 2 by solving Eq. (17) at fixed intervals of frequency (using a 10-MHz step size) for values of k_x between 0 and 6000. The dark blue curves represent solutions of the MEE coupled waveguide. Additionally, we examine the "reference" dispersion curves by setting all piezoelectric and piezomagnetic coefficients to zero and recalculating the field solutions. The reference dispersion curves, see cyan curves Fig. 2, resemble those of a typical EM waveguide.

Comparing the two sets of dispersion curves, we can see some similarities as well as clear differences. Each branch representing a particular guided mode has a cut-off frequency, at which k_x is close to 0, and in general, the cut-off frequencies of the MEE modes are higher than the reference, non-MEE material, modes. As frequency increases, k_x tends to become more linear and $\partial\omega/\partial k_x$ approaches the respective modal phase velocity. In Fig. 2, one noticeable difference across most frequency ranges as well as below the cut-off frequency of 690 MHz is that k_x increases rapidly such that $\partial\omega/\partial k_x$ approaches zero periodically. Considering $k_x^2 + k_z^2 = k^2$ where the wave number k at a given frequency is determined by material properties, this anomaly is directly related to the fact that k_z becomes imaginary and its magnitude grows steeply at the frequency regions highlighted by orange dashed lines in Fig. 2. To further understand this phenomenon, we note

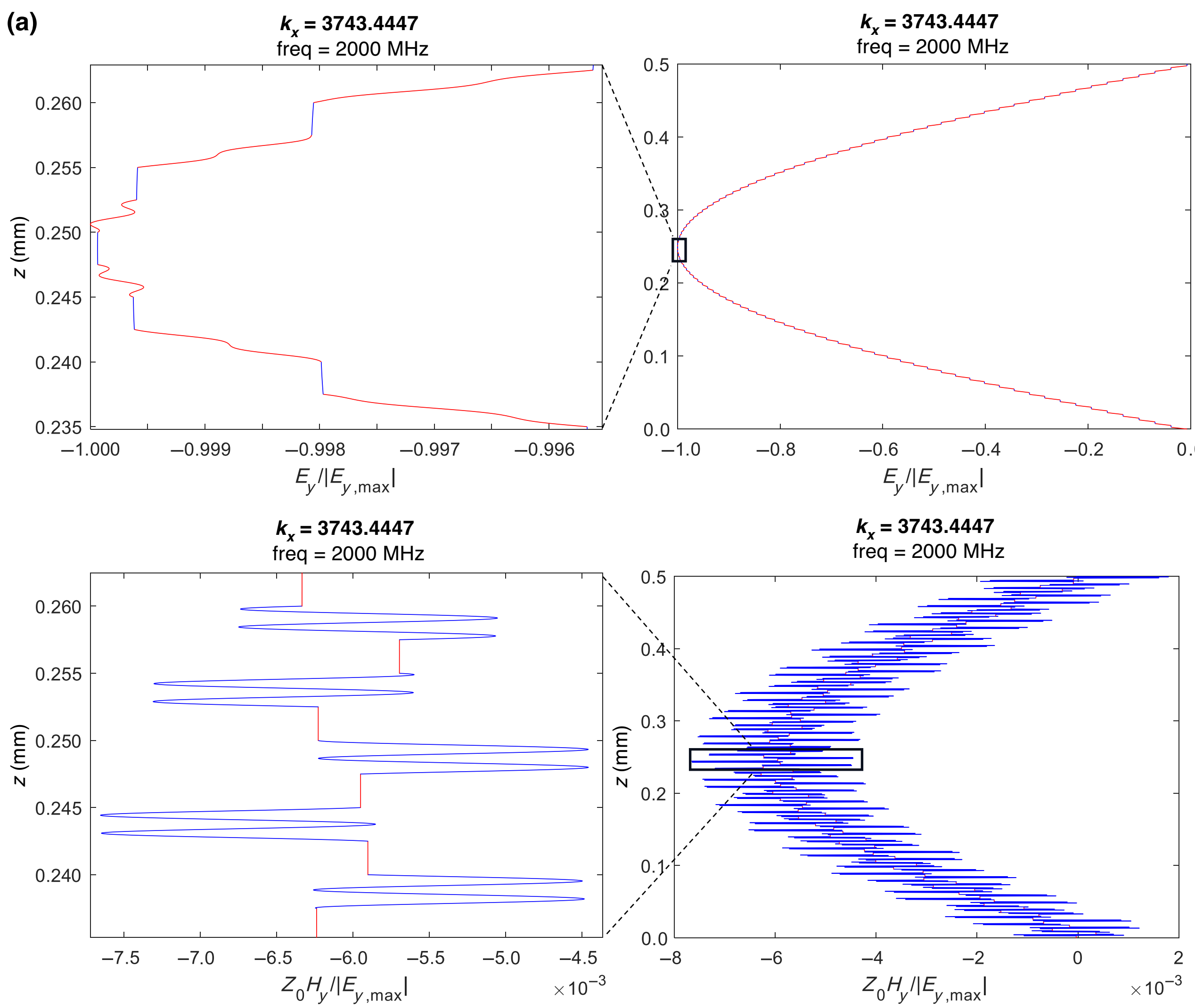

FIG. 3. (Continued.)

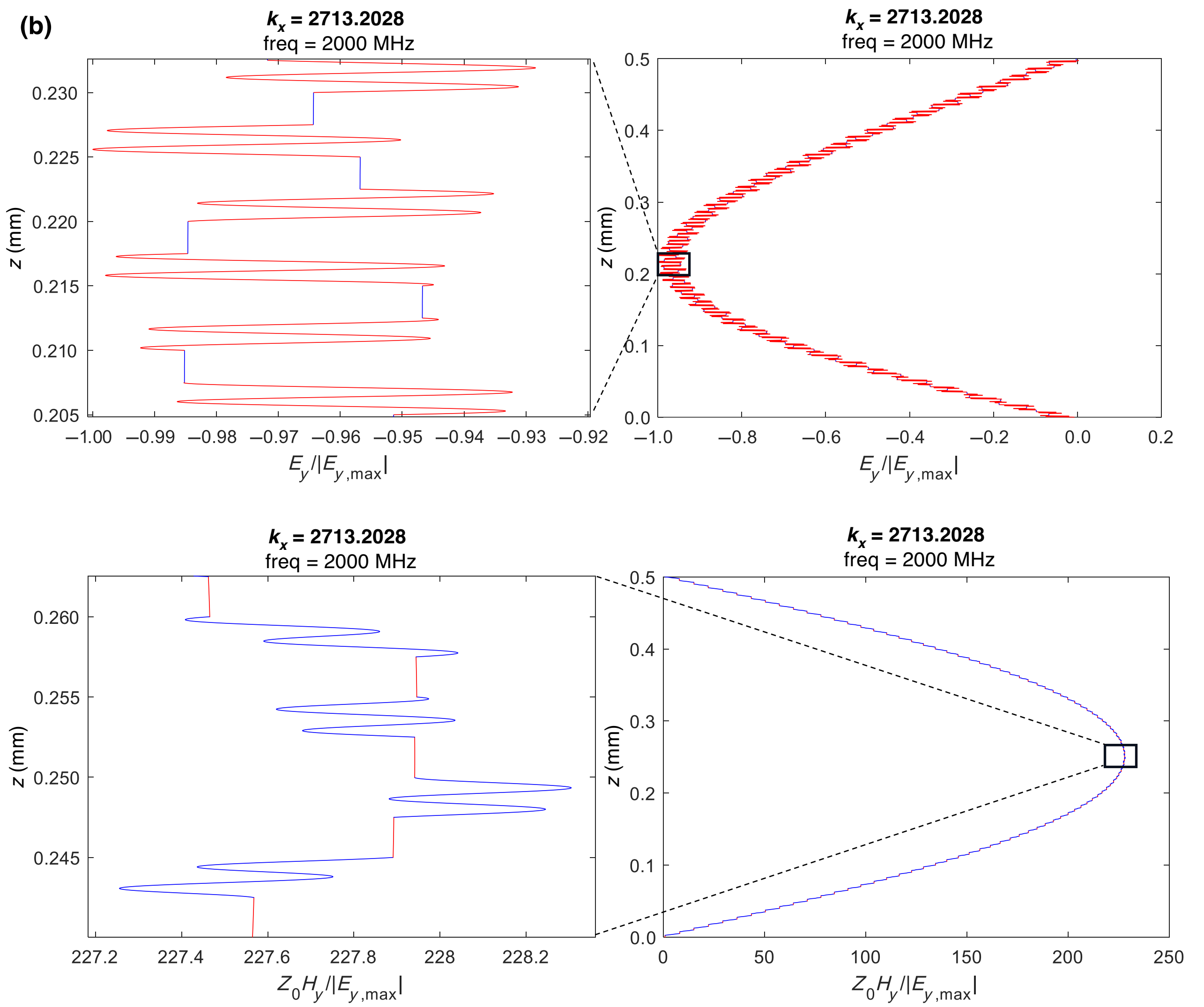

FIG. 3. (Continued.)

that for a guided mode to exist in a waveguide, the transverse resonance condition must be satisfied, and it suffices to study only the wave component traveling along the z direction, which must interfere with itself constructively. To this end, we can solve for the one-dimensional (1D) Helmholtz equation, whose solution is given by Eq. (4) in Ref. [15]:

$$S_5 \approx \sum_n \frac{G_n^2}{\omega^2 \rho s_{55} - G_n^2}(-d_{15}g_{1n}E_x - q_{15}g_{2n}H_x)e^{jG_nz}, \tag{18}$$

where $G_n = n\pi/t$ and $g_1(z) \approx \sum_n g_{1n}e^{jG_nz}$, $g_2(z) \approx \sum_n g_{2n}e^{jG_nz}$ are Fourier expansion forms of two rectangular functions: $g_1 = 1$, $g_2 = 0$ in piezoelectric layers and $g_1 = 0$, $g_2 = 1$ in piezomagnetic layers; ρ, the density, and s_{55}, which is inversely proportional to the shear modulus representing the shear stiffness in the 1–3 plane in the material coordinate system (which is aligned with the global coordinate system in this case, and therefore the aforementioned 1–3 plane is indeed the x-z plane, where the guided wave propagates), are the average of corresponding piezoelectric and piezomagnetic parameters (note that the two materials considered here, $BaTiO_3$ and $CoFe_2O_4$, have similar values for ρ and s_{55}). For a certain frequencies, corresponding to m such that $\omega \to \omega_m = m\pi/\left(t\sqrt{\rho s_{55}}\right)$, the denominator in Eq. (18) becomes small, increasing S_5 and resulting in negative wave numbers, as explained in detail in Ref. [16]. Such increases in S_5 enhance the ME coupling since the corresponding frequencies are closer to resonance; consequently, both the piezoelectric and piezomagnetic coupling are strengthened. Additionally, by taking advantage of the low group velocity, $v_g = \partial\omega/\partial k_x \to 0$, we may create slow-wave structures using such MEE waveguides.

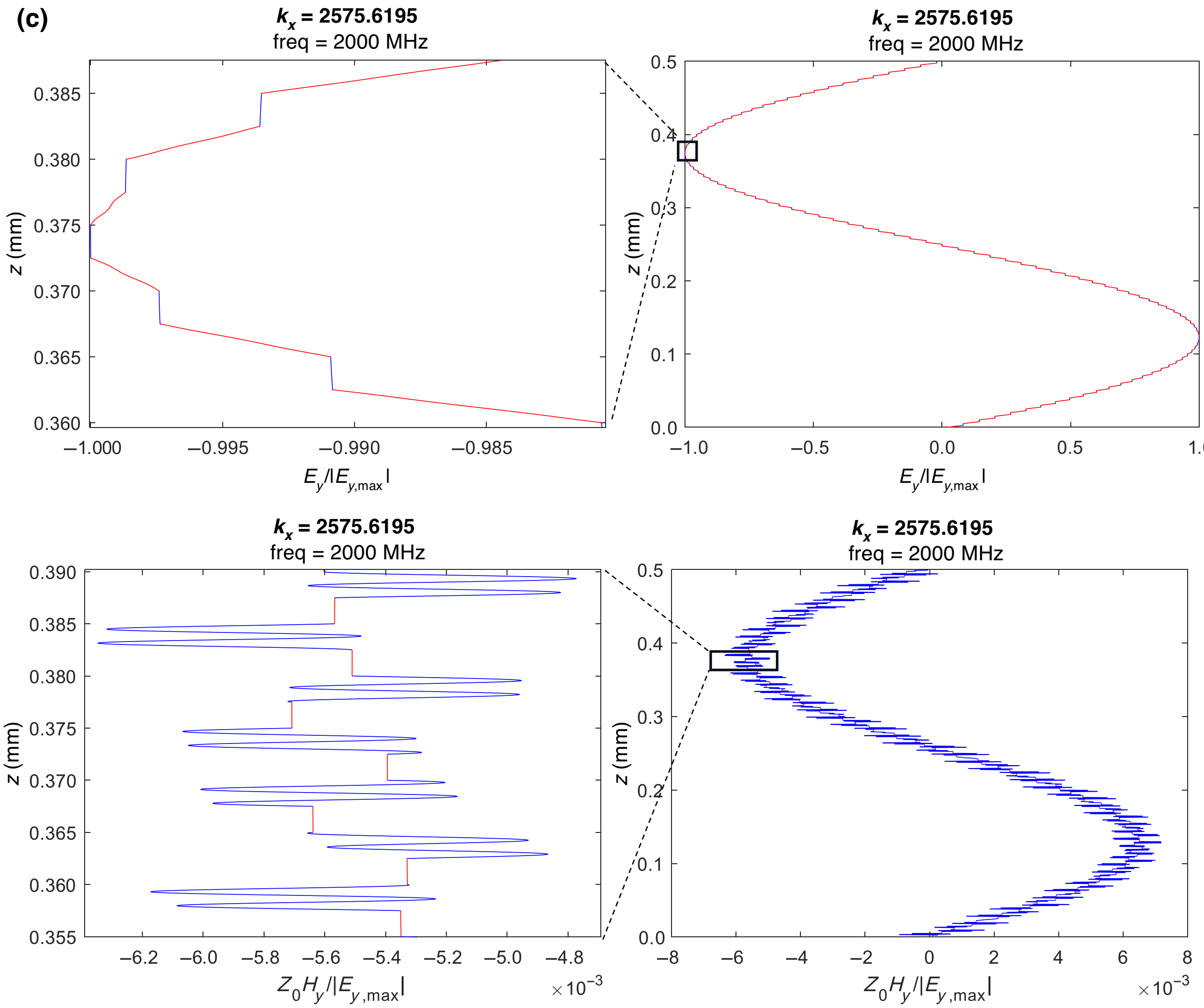

FIG. 3. (Continued.)

To understand the electromagnetic behavior of the waveguide, we examine the electric and magnetic fields produced through a cross section of the dispersion space. The normalized fields associated with the four points identified in Fig. 2 at 2 GHz are plotted in Fig. 3. Each profile of E_y and H_y represent four different guided modes in the MEE waveguide at 2 GHz. Due to the piezoelectric coupling coefficient d_{24}, E_y is coupled to the shear strain component S_4, which is then transferred to the piezomagnetic phase further exciting H_y. Likewise, the strain coupling causes H_y to excite E_y. This is unlike conventional slab waveguides where the modes can be categorized as TE modes ($E_y \neq 0, H_y = 0$) or TM modes ($H_y \neq 0, E_y = 0$).

Thus, in the MEE waveguide, all the guided modes exhibit nonzero E_y and H_y. In some cases, however, as seen in Figs. 3(a) and 3(c), the magnitude of the "extra" H_y term is 4 orders of magnitude smaller than conventional E_y. Consequently, this perturbed TE mode can be considered quasi-TE. In contrast, for other modes, as shown in Figs. 3(b) and 3(d), the strain-induced H_y and E_y fields are comparable in magnitude. We refer to these as hybrid modes.

Some further observations on the mode shapes are noteworthy. Comparing the E_y profiles in Figs. 3(a) and 3(c), as well as the H_y profile in in Figs. 3(b) and 3(d), we notice the half-cycle and full-cycle sinusoidal forms, respectively, which are characteristic of different mode order, just as in the conventional slab waveguide for $n = 0$ and $n = 1$. In addition, E_y, suppressing $\exp(-j\,k_x x)$, is $E_y = \left[\left(E_{y0}^{+}e^{-jk_z^{\mathrm{EM}}z} + E_{y0}^{-}e^{jk_z^{\mathrm{EM}}z}\right) + \left(E_y^{+\prime}e^{-jk_z^{\mathrm{ela}}z} + E_y^{-\prime}e^{jk_z^{\mathrm{ela}}z}\right)\right]$. The first term is the sum of the two quasi-EM modes and the second term is the sum of the perturbations from the quasiacoustic modes [17] whose magnitude $|E_y^{\pm\prime}| \ll |E_{y0}^{\pm}|$. The quasi-EM modes are the dominant component of E_y in the piezoelectric layers. Given that the layer thickness

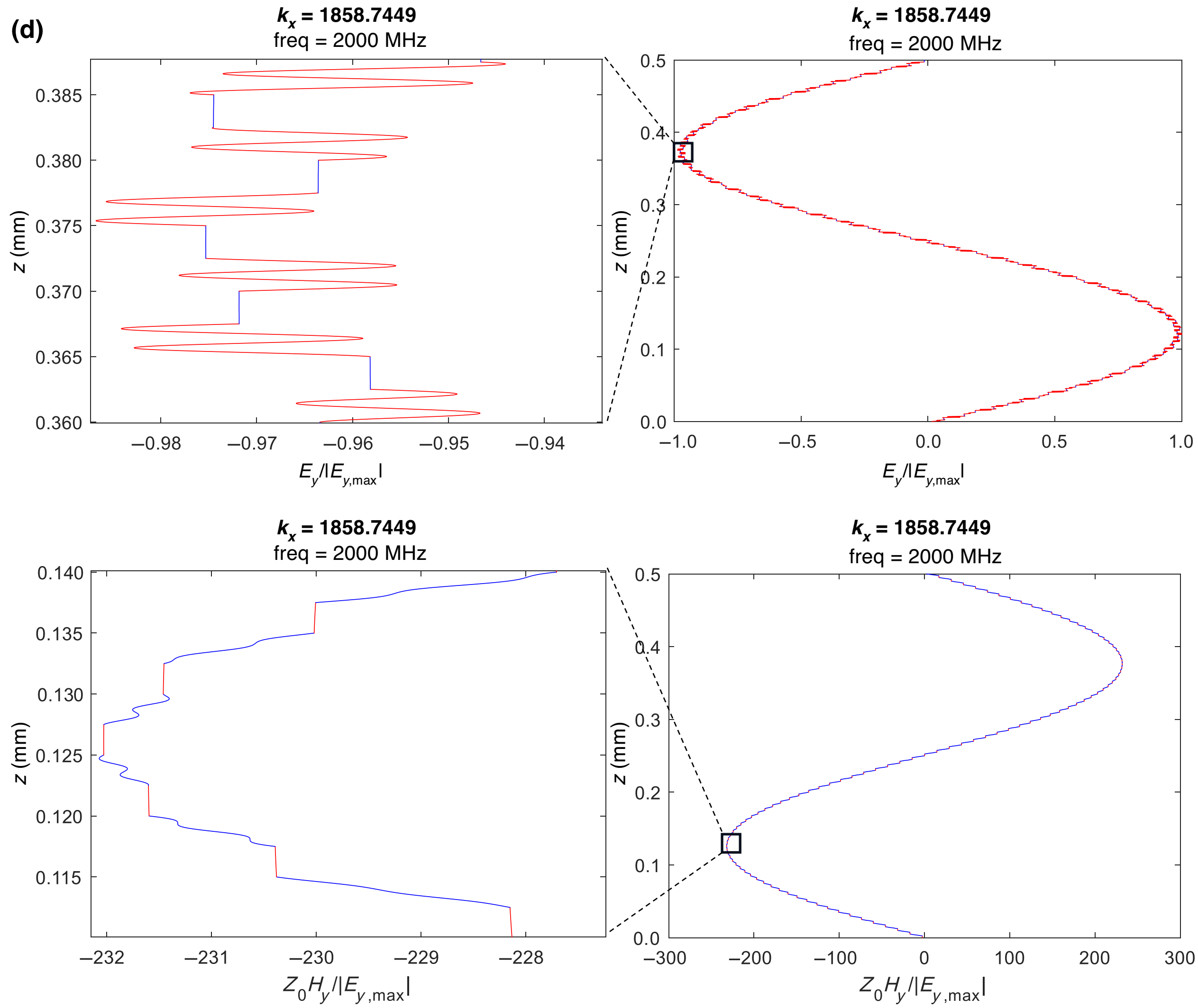

FIG. 3. The EM field profiles of E_y and H_y of the four points highlighted in Fig. 2: (a) P1 ($k_x = 3743.4\ \mathrm{m}^{-1}$), quasi-TE mode of order $n = 0$; (b) P2 ($k_x = 2713.2\ \mathrm{m}^{-1}$), hybrid mode of order $n = 0$; (c) P3 ($k_x = 2575.6\ \mathrm{m}^{-1}$), quasi-TE mode of order $n = 1$; (d) P4 ($k_x = 1858.7\ \mathrm{m}^{-1}$), hybrid mode of order $n = 1$. The fields in the piezoelectric layers and in the piezomagnetic layers are represented by blue, red lines, respectively. The fields in the maximum-magnitude regions are enlarged to show the profiles in constituent layers. The scale of all the plots is normalized with respect to the largest magnitude of E_y of the respective mode, and $Z_0 = 376.7\ \Omega$, the vacuum intrinsic impedance, is multiplied with H_y for nondimensionalization.

is much smaller than the quasi-EM modes' wavelength, we observe a linear variation of E_y. Likewise, in the piezomagnetic layer, H_y is linear.

It is instructive to analyze in greater detail characteristics of the dispersion graph previously shown in Fig. 2. For this purpose, we analyze the first resonant mode area between 500 and 620 MHz. Mode shapes for different k_x values in this frequency range are categorized and similar modes are grouped together as displayed in Fig. 4. The dots in Fig. 4(a) indicate solutions of Eq. (17) across the selected frequency spectrum. For each frequency, solutions of k_x in the range 0–6000 are plotted. Each solution is then analyzed to determine the corresponding mode shape. Prototypical mode shapes are plotted in Figs. 4(b)–4(d) for mode numbers 0–2, respectively. Modes of similar order are connected by dashed lines. For example, mode 0 solutions, $n = 0$, starting with the point at $k_x = 647.05[1/\mathrm{m}], f = 560.00[\mathrm{MHz}]$ are connected by a green dashed line and mode 1, with $n = 1$, starting at $k_x = 1181.76[1/\mathrm{m}], f = 566.25[\mathrm{MHz}]$ are shown connected with a cyan dashed line. Higher-order mode groups ($n \geq 2$) are connected with red dashed lines. All the mode groups exhibit similar sinusoidal patterns throughout the stack and within each layer, similar to what is shown in Fig. 3, the EM fields also vary sinusoidally on the scale of the elastic vibration. As mode order increases, the modes become less dispersive; indeed, for $n \geq 2$, k_x is almost linearly dependent on frequency. We also note that there exists a significant difference in the group velocity between the fundamental modes at $n = 0$ and other higher-order modes, including $n = 1$. For instance, the mode of Fig. 4(b) has $\partial\omega/\partial k_x = 2.6 \times 10^5$ m/s, whereas the group velocity associated with Fig. 4(d) is only 9.86×10^3 m/s, which is on the same order of magnitude of the elastic wave and quite slow for a propagating EM wave.

Nonreciprocal wave propagation is one of the properties of bianisotropic media [18], which can be practically realized by temporally or spatially modulated structures. Here we are going to demonstrate that an MEE waveguide can achieve remarkable nonreciprocity as well, by making use of the anisotropy of the piezoelectric and piezomagnetic materials. Solids with ME coupled constitutive parameters are characterized by $\underline{D} = \boldsymbol{\varepsilon}^{DB}\underline{E} + \boldsymbol{\xi}^{DB}\underline{H}$, $\underline{B} = \boldsymbol{\zeta}^{DB}\underline{E} + \boldsymbol{\mu}^{DB}\underline{H}$. The superscript "$DB$" indicates that the constitutive parameters $\underline{D}$ and $\underline{B}$ are expressed in terms of the independent fields $\underline{E}$ and $\underline{H}$. Specifically, for waves traveling along the x direction, nonreciprocity arises when $\xi_{23}^{DB} \neq 0$. It is shown in Ref. [19] that the electric field contains a term proportional to the cross product of the wave vector and the magnetoelectrically induced magnetization via ξ_{23}^{DB} coupling. Consequently, the E-field intensity depends on the propagation direction. Such coupling is controlled in an MEE composite, through strain mediation. In the present cause, aligning the d_{24} axis of the piezoelectric coupling matrix and with the q_{34} axis of the piezomagnetic coupling matrix, the ME effect is maximized. This is done by rotating the material coordinate system of $CoFe_2O_4$ by a set of Euler angles $\begin{bmatrix}\phi & \theta & \psi\end{bmatrix} = \begin{bmatrix}0 & 2.77 & 0\end{bmatrix}$, while $BaTiO_3$'s material coordinate system remains aligned with the global coordinate system. To facilitate strain transfer between adjacent layers, we set layer thickness, for both piezoelectric and piezomagnetic materials, to be 1.25 um. This is half the thickness used in the previous analysis, and the total number of layers is increased to 400 so the entire stack remains 0.5 mm thick. Following the same procedure as before, we calculate the dispersion curves for both $k_x > 0$ and $k_x < 0$, with negative k_x values indicating solutions for

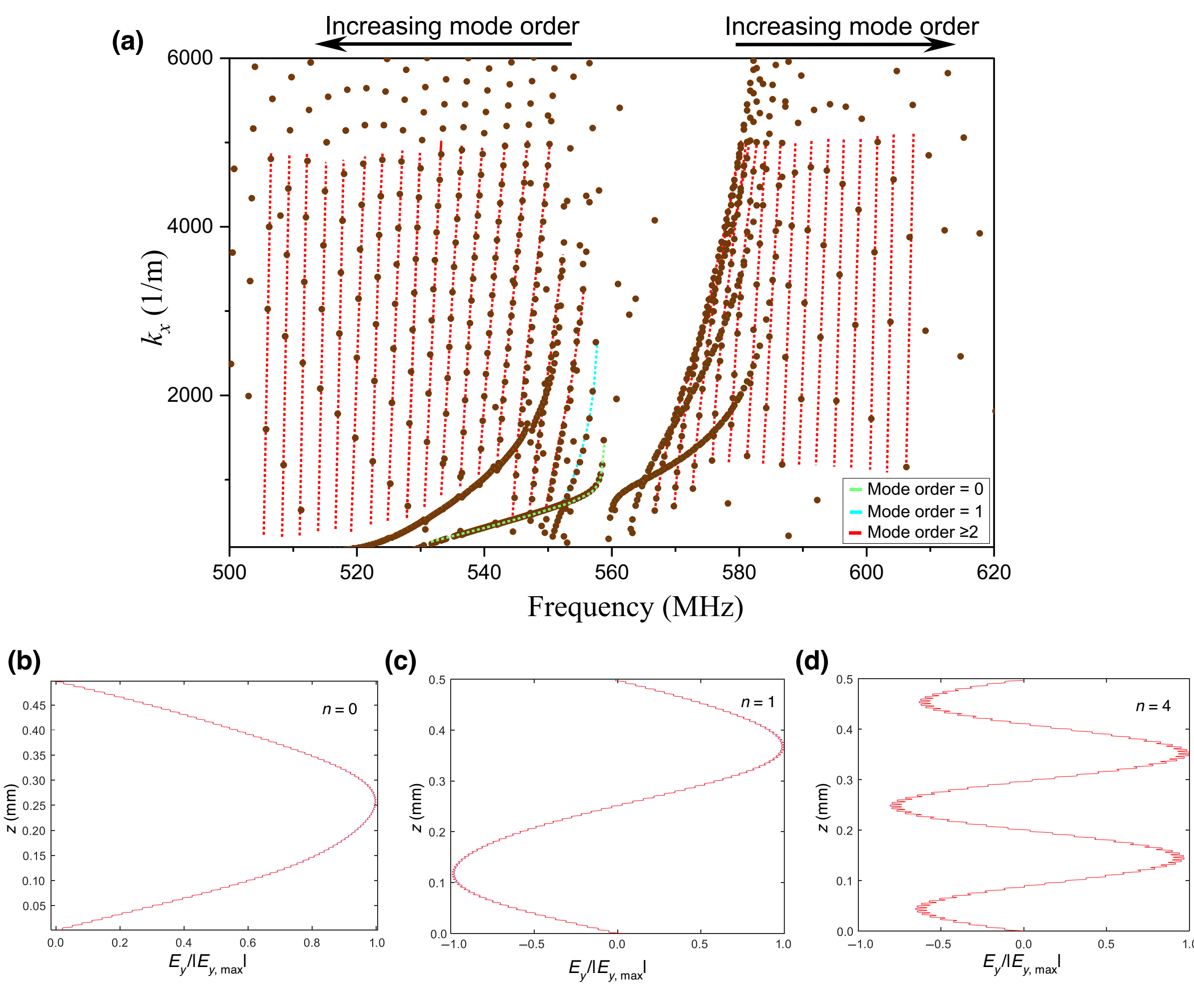

FIG. 4. (a) Dispersion curves of the resonance region between 500 and 620 MHz. Different modes are grouped by dashed lines of different colors, of which the normalized E_y profiles are shown for mode order (b) $n = 0$, (c) $n = 1$, (d) $n = 4$.

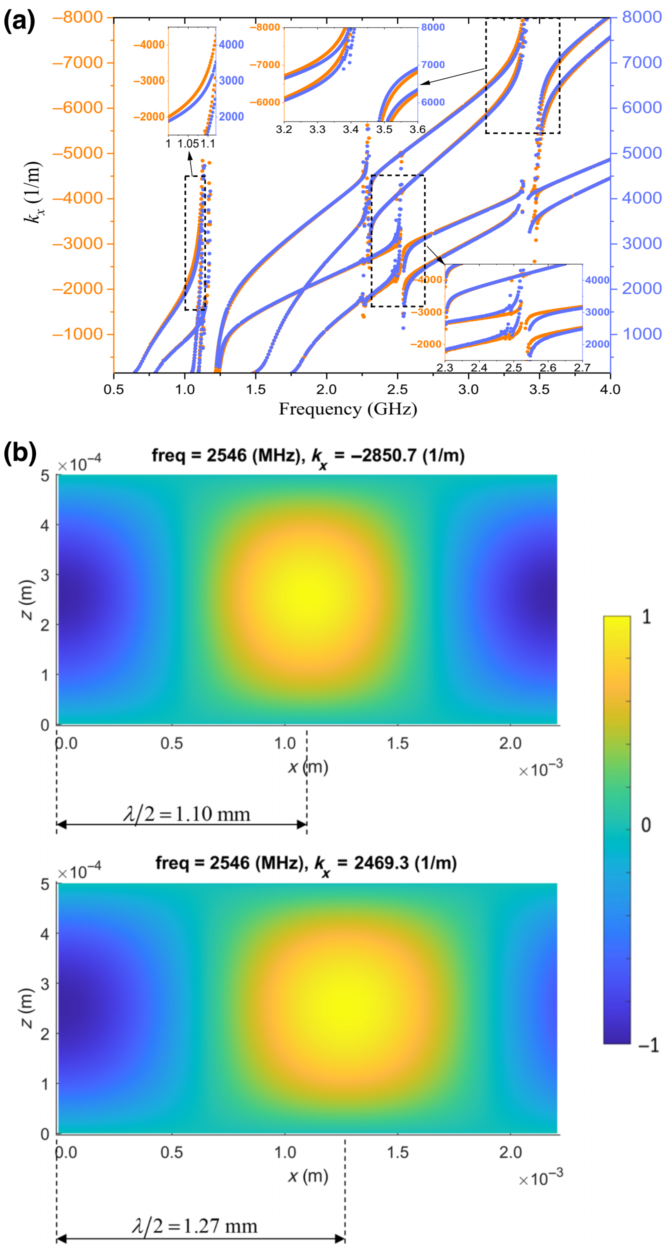

FIG. 5. (a) Dispersion curves of an MEE waveguide exhibiting nonreciprocity: blue and orange curves denote $k_x > 0$ and $k_x < 0$, respectively. The stack of the waveguide contains 400 layers, each of which is 1.25 um thick. The insets present noticeable difference in the magnitude of k_x for waves traveling in $+x$ ($k_x > 0$) and $-x$ axis ($k_x < 0$) around the resonance region. (b) E_y distribution of the fundamental hybrid mode at 2546 MHz in a section of the MEE waveguide for $k_x > 0$ (wave propagating at $+x$ axis) and $k_x < 0$ (wave propagating at $-x$ axis).

the negative x direction. Dispersion curves for lower order modes, $n = 0$ and $n = 1$, are plotted in Fig. 5(a). Comparing Fig. 5(a) with the dispersion curve in Fig. 2, the period of the resonance doubles from 0.55 GHz to approximately 1.1 GHz, as the layer thickness is halved from 2.5 um to 1.25 um.[20] Most notably, the dispersion curves of $k_x > 0$ do not overlap with those of $k_x < 0$. Since the wave velocity varies depending on the direction along which the waves travel (in this case, $+x$ axis or $-x$ axis), we clearly have nonreciprocal modes. This is known as nonreciprocal directional dichroism (NDD), which refers to the difference in the phase velocity for wave propagation in one direction versus the reverse direction. The occurrence of NDD requires that both time reversal and spatial inversion should be simultaneously broken [21].

Various approaches to reducing the symmetry in the materials have been researched intensively in single-phase multiferroics, which generally exhibit weak ME coupling. Use of a cryogenic environment or external bias fields are often employed to produce notable ME effects. On the other hand, MEE composites can exhibit sizable ME coupling without these special conditions. Moreover, nonreciprocal effects become pronounced close to resonance as indicated by Eq. (18). The insets shown in Fig. 5(a) highlight the difference in values of k_x in the positive x direction versus the $-x$ direction. As an example, E_y is plotted in Fig. 5(b) for mode zero, $n = 0$, at 2546 MHz. The wave number $k_x = 2569.3$ [1/m] in the forward direction and $k_x = -2850.7$ [1/m] in the negative x direction. This amounts to 14.2% difference in phase velocity.

IV. CONCLUSION

In summary, we have derived the governing equations for the EM waves in an MEE solid and made use of the transfer-matrix method to obtain the dispersion curves of an MEE waveguide stacked with piezoelectric and piezomagnetic layers. Like conventional slab EM waveguides, the profile of the guided modes in MEE waveguide shows sinusoidal patterns. The difference due to the mechanical coupling in MEE solid, however, is also remarkable. It is shown that for all guided modes, the y component of the electric field E_y, and that of the magnetic field, H_y are nonzero, but their magnitude relative to each other varies with the mode. Based on the relative strength of the field components, modes are categorized into quasi-TE modes (H_y is negligible compared to E_y) and hybrid modes (H_y is comparable to E_y). Moreover, there exist periodic resonance regions where the group velocity $\partial\omega/\partial k_x$ approaches zero (i.e., frozen modes) as the vertical component of the wave vector k_z becomes imaginary. Further, examination of the resonance regions reveals that modes of various orders are present with lower-order modes ($n = 0, 1$) being highly dispersive, and high-order modes ($n \geq 2$) are essentially dispersionless with group velocities on the order of 10^3–10^4 m/s. Lastly, we show nonreciprocal wave modes in the MEE slab waveguide phase velocity 14.2% faster along $+x$ axis compared to propagation along $-x$ axis for frequencies near the resonance region. This corresponds to the strongest strain-mediated magnetoelectric coupling. The findings in this study open up possibilities of utilizing MEE materials for slow-wave waveguides that facilitate size reduction in radio-frequency integration circuits (RFIC), and for compact nonreciprocal wave transmission components such as circulators, isolators and gyrators that are likely to replace the bulky and externally biased ones in use today.

APPENDIX

$\mathbf{Q}$ in Eq. (9) is a 15×15 matrix as shown below and can be partitioned into four block matrices:

$$
\mathbf{Q} = \left[\begin{array}{ccccc|cccccccccc}
s_{11} & s_{12} & s_{16} & d_{31} & q_{31} & s_{13} & 0 & s_{14} & 0 & s_{15} & k_x/\omega & d_{11} & q_{21} & d_{21} & q_{11} \\
s_{21} & s_{22} & s_{26} & d_{32} & q_{32} & s_{23} & 0 & s_{24} & k_y/\omega & s_{25} & 0 & d_{12} & q_{22} & d_{22} & q_{12} \\
s_{61} & s_{62} & s_{66} & d_{36} & q_{36} & s_{63} & 0 & s_{64} & k_x/\omega & s_{65} & k_y/\omega & d_{16} & q_{26} & d_{26} & q_{16} \\
d_{31} & d_{32} & d_{36} & \varepsilon_{33} & \xi_{33} & d_{33} & 0 & d_{34} & 0 & d_{35} & 0 & \varepsilon_{31} & k_x/\omega + \xi_{32} & \varepsilon_{32} & -k_y/\omega + \xi_{31} \\
q_{31} & q_{32} & q_{36} & \zeta_{33} & \mu_{33} & q_{33} & 0 & q_{34} & 0 & q_{35} & 0 & k_y/\omega + \zeta_{31} & \mu_{32} & -k_x/\omega + \zeta_{32} & \mu_{31} \\
\hline
s_{31} & s_{32} & s_{36} & d_{33} & q_{33} & s_{33} & k_z/\omega & s_{34} & 0 & s_{35} & 0 & d_{13} & q_{23} & d_{23} & q_{13} \\
0 & 0 & 0 & 0 & 0 & k_z/\omega & \rho & k_y/\omega & 0 & k_x/\omega & 0 & 0 & 0 & 0 & 0 \\
s_{41} & s_{42} & s_{46} & d_{34} & q_{34} & s_{43} & k_y/\omega & s_{44} & k_z/\omega & s_{45} & 0 & d_{14} & q_{24} & d_{24} & q_{14} \\
0 & k_y/\omega & k_x/\omega & 0 & 0 & 0 & 0 & k_z/\omega & \rho & 0 & 0 & 0 & 0 & 0 & 0 \\
s_{51} & s_{52} & s_{56} & d_{35} & q_{35} & s_{53} & k_x/\omega & s_{54} & 0 & s_{55} & k_z/\omega & d_{15} & q_{25} & d_{25} & q_{15} \\
k_x/\omega & 0 & k_y/\omega & 0 & 0 & 0 & 0 & 0 & 0 & k_z/\omega & \rho & 0 & 0 & 0 & 0 \\
d_{11} & d_{12} & d_{16} & \varepsilon_{13} & k_y/\omega + \xi_{13} & d_{13} & 0 & d_{14} & 0 & d_{15} & 0 & \varepsilon_{11} & -k_z/\omega + \xi_{12} & \varepsilon_{12} & \xi_{11} \\
q_{21} & q_{22} & q_{26} & k_x/\omega + \zeta_{23} & \mu_{23} & q_{23} & 0 & q_{24} & 0 & q_{25} & 0 & -k_z/\omega + \zeta_{21} & \mu_{22} & \zeta_{22} & \mu_{21} \\
d_{21} & d_{22} & d_{26} & \varepsilon_{23} & -k_x/\omega + \xi_{23} & d_{23} & 0 & d_{24} & 0 & d_{25} & 0 & \varepsilon_{21} & \xi_{22} & \varepsilon_{22} & k_z/\omega + \xi_{21} \\
q_{11} & q_{12} & q_{16} & -k_y/\omega + \zeta_{13} & \mu_{13} & q_{13} & 0 & q_{14} & 0 & q_{15} & 0 & \zeta_{11} & \mu_{12} & k_z/\omega + \zeta_{12} & \mu_{11}
\end{array}\right]
$$

$$
= \left[\begin{array}{c|c} \mathbf{Q}_{11} & \mathbf{Q}_{12} \\ \hline \mathbf{Q}_{12}^T & \mathbf{Q}_{22} \end{array}\right]
$$

where $\mathbf{Q}_{22}$ can be further split into two matrices: $\mathbf{Q}_{22}(k_x, k_y, k_z, \omega) = \mathbf{Q}_{22}^z(k_z, \omega) + \mathbf{Q}_{22}^c(k_x, k_y, \omega)$

$$
\mathbf{Q}_{22}^z = \begin{bmatrix}
0 & k_z/\omega & 0 & 0 & 0 & 0 & 0 & 0 & 0 & 0 \\
k_z/\omega & 0 & 0 & 0 & 0 & 0 & 0 & 0 & 0 & 0 \\
0 & 0 & 0 & k_z/\omega & 0 & 0 & 0 & 0 & 0 & 0 \\
0 & 0 & k_z/\omega & 0 & 0 & 0 & 0 & 0 & 0 & 0 \\
0 & 0 & 0 & 0 & 0 & k_z/\omega & 0 & 0 & 0 & 0 \\
0 & 0 & 0 & 0 & k_z/\omega & 0 & 0 & 0 & 0 & 0 \\
0 & 0 & 0 & 0 & 0 & 0 & 0 & -k_z/\omega & 0 & 0 \\
0 & 0 & 0 & 0 & 0 & 0 & -k_z/\omega & 0 & 0 & 0 \\
0 & 0 & 0 & 0 & 0 & 0 & 0 & 0 & 0 & k_z/\omega \\
0 & 0 & 0 & 0 & 0 & 0 & 0 & 0 & k_z/\omega & 0
\end{bmatrix}
$$

$$
\mathbf{Q}_{22}^c = \begin{bmatrix}
s_{33} & 0 & s_{34} & 0 & s_{35} & 0 & d_{13} & q_{23} & d_{23} & q_{13} \\
0 & \rho & k_y/\omega & 0 & k_x/\omega & 0 & 0 & 0 & 0 & 0 \\
s_{43} & k_y/\omega & s_{44} & 0 & s_{45} & 0 & d_{14} & q_{24} & d_{24} & q_{14} \\
0 & 0 & 0 & 0 & 0 & 0 & 0 & 0 & 0 & 0 \\
s_{53} & k_x/\omega & s_{54} & 0 & s_{55} & 0 & d_{15} & q_{25} & d_{25} & q_{15} \\
0 & 0 & 0 & 0 & 0 & \rho & 0 & 0 & 0 & 0 \\
d_{13} & 0 & d_{14} & 0 & d_{15} & 0 & \varepsilon_{11} & \xi_{12} & \varepsilon_{12} & \xi_{11} \\
q_{23} & 0 & q_{24} & 0 & q_{25} & 0 & \zeta_{21} & \mu_{22} & \zeta_{22} & \mu_{21} \\
d_{23} & 0 & d_{24} & 0 & d_{25} & 0 & \varepsilon_{21} & \xi_{22} & \varepsilon_{22} & \xi_{21} \\
q_{13} & 0 & q_{14} & 0 & q_{15} & 0 & \zeta_{11} & \mu_{12} & \zeta_{12} & \mu_{11}
\end{bmatrix}.
$$

[1] G. Srinivasan, E. T. Rasmussen, B. J. Levin, and R. Hayes, Magnetoelectric effects in bilayers and multilayers of magnetostrictive and piezoelectric perovskite oxides, Phys. Rev. B **65**, 134402 (2002).

[2] M. Ghidini, R. Pellicelli, J. L. Prieto, X. Moya, J. Soussi, J. Briscoe, S. Dunn, and N. Mathur, Non-volatile electrically-driven repeatable magnetization reversal with no applied magnetic field, Nat. Commun. **4**, 1453 (2013).

[3] Y. J. Wang, D. Gray, D. Berry, J. Q. Gao, M. H. Li, J. F. Li, and D. Viehland, An extremely low equivalent magnetic noise magnetoelectric sensor, Adv. Mater. **23**, 4111 (2011).

[4] J. L. Drobitch, A. De, K. Dutta, P. K. Pal, A. Adhikari, A. Barman, and S. Bandyopadhyay, extreme subwavelength magnetoelastic electromagnetic antenna implemented with multiferroic nanomagnets, Adv. Mater. Technol. **5**, 2000316 (2020).

[5] C. He, X.-C. Sun, X.-P. Liu, M.-H. Lu, Y. Chen, L. Feng, and Y.-F. Chen, Photonic topological insulator with broken time-reversal symmetry, Proc. Natl. Acad. Sci. U. S. A. **113**, 4924 (2016).

[6] Y. Lin, N. Cai, J. Zhai, G. Liu, and C.-W. Nan, Giant magnetoelectric effect in multiferroic laminated composites, Phys. Rev. B **72**, 012405 (2005).

[7] A. Mazzamurro, Y. Dusch, P. Pernod, O. Matar, A. Addad, A. Talbi, and N. Tiercelin, Giant magnetoelastic coupling in a Love acoustic waveguide based on $TbCo_2/FeCo$ nanostructured film on ST-cut quartz, Phys. Rev. Appl. **13**, 044001 (2020).

[8] J. Chen, E. Pan, and H. Chen, Wave propagation in magneto-electro-elastic multilayered plates, Int. J. Solids Struct. **44**, 1073 (2007).

[9] M. J. S. Lowe, Matrix techniques for modeling ultrasonic waves in multilayered media, IEEE Trans. Ultrason. Ferroelectr. Freq. Control **42**, 525 (1995).

[10] J. Chilwell and I. Hodgkinson, Thin-films field-transfer matrix theory of planar multilayer waveguides and reflection from prism-loaded waveguides, J. Opt. Soc. Am. A **1**, 742 (1984).

[11] J. A. Kong, *Electromagnetic Wave Theory* (Wiley-Interscience, New York, 1986), pp. 51.

[12] Strictly speaking, it is not possible to tell whether $\mathbf{Q}_{11}$is invertible without knowing the material parameters. However, from thermodynamic considerations and noting the particular material parameters that appear in $\mathbf{Q}_{11}$, it is certainly invertible for all “normal” materials. For the materials studied here, i.e., $BaTiO_3$ and $CoFe_2O_4$, $\mathbf{Q}_{11}$ is verified to be invertible.

[13] S. Keller, PhD Dissertation, University of California, Los Angeles, Los Angeles, CA, 2013.

[14] J.-Y. Kim, Micromechanical analysis of effective properties of magneto-electro-thermo-elastic multilayer composites, Int. J. Eng. Sci. **49**, 1001 (2011).

[15] J. Zhao, R.-C. Yin, T. Fan, M.-H. Lu, Y.-F. Chen, Y.-Y. Zhu, S.-N. Zhu, and N.-B. Ming, Coupled phonon polaritons in a piezoelectric-piezomagnetic superlattice, Phys. Rev. B **77**, 075126 (2008).

[16] H. Liu, S. N. Zhu, Y. Y. Zhu, Y. F. Chen, N. B. Ming, and X. Zhang, Piezoelectric–piezomagnetic multilayer with simultaneously negative permeability and permittivity, Appl. Phys. Lett. **86**, 102904 (2005).

[17] J. J. Kyame, Wave propagation in piezoelectric crystals, J. Acoust. Soc. Am. **21**, 159 (1949).

[18] X. Wang, G. Ptitcyn, V. S. Asadchy, A. Díaz-Rubio, M. S. Mirmoosa, S. Fan, and S. A. Tretyakov, Nonreciprocity in bianisotropic systems with uniform time modulation, Phys. Rev. Lett. **125**, 266102 (2020).

[19] S. Keller and G. Carman, Electromagnetic wave propagation in (bianisotropic) magnetoelectric materials, J. Intell. Mater. Syst. Struct. **24**, 651 (2012).

[20] At the second region of discontinuity (between 2.2 and 2.6 GHz), different branches break at different frequencies: 2.28 GHz for the quasi-TE modes, 2.52 GHz for the hybrid modes. This is mainly because the stiffness matrix of the piezomagnetic layer is changed after rotation, which is no longer transversely isotropic, $s_{44}^{\mathrm{PM}} = 2.05 \times 10^{-11}, s_{55}^{\mathrm{PM}} = 2.15 \times 10^{-11}$, as opposed to $s_{44}^{\mathrm{PE}} = s_{55}^{\mathrm{PE}} = 2.32 \times 10^{-11}$ in the piezoelectric layer.

[21] I. Kézsmárki, N. Kida, H. Murakawa, S. Bordács, Y. Onose, and Y. Tokura, Enhanced directional dichroism of terahertz light in resonance with magnetic excitations of the multiferroic $Ba_2CoGe_2O_7$ oxide compound, Phys. Rev. Lett. **106**, 057403 (2011).